CMOS-compatible all-dielectric metalens for improving pixel photodetector arrays

E Mikheeva, J.-B Claude, M Salomoni, Jérôme Wenger, Julien Lumeau, R. Abdeddaim, A Ficorella, A Gola, G Paternoster, M. Paganoni, et al.

CMOS-compatible all-dielectric metalens for improving pixel photodetector arrays

E. Mikheeva,[1,2] J.-B. Claude,[1] M. Salomoni,[3,4] J. Wenger,[1] J. Lumeau,[1] R. Abdeddaim,[1] A. Ficorella,[5] A. Gola,[5] G. Paternoster,[5] M. Paganoni,[3] E. Auffray,[4] P. Lecoq,[4,6] and S.Enoch[1,a)]

[1)] *Aix Marseille Univ, CNRS, Centrale Marseille, Institut Fresnel, 13013 Marseille, France*

[2)] *Multiwave Imaging, 2 Marc Donadille, 13453 Marseille, France*

[3)] *University of Milano-Bicocca. Piazza dell'Ateneo Nuovo, 1, 20126 Milan, Italy*

[4)] *European Organization for Nuclear Research (CERN), 1211, Geneva, Switzerland*

[5)] *Fondazione Bruno Kessler. Via Santa Croce, 77, 38122, Trento, Italy*

[6)] *Multiwave Metacrystal SA, 34 Route de la Galaise, 1228, Geneva, Switzerland*

(Dated: 24 October 2020)

Metasurfaces and, in particular, metalenses have attracted large interest and enabled various applications in the near-infrared and THz regions of the spectrum. However, metalens design in the visible range stays quite challenging due to the smaller nanostructuring scale and the limited choice of lossless CMOS-compatible materials. We develop a simple, yet efficient design of a polarization-independent, broadband metalens suitable for many CMOS-compatible fabrication techniques and materials and implement it for the visible spectral range using niobium pentoxide Nb_2O_5. The produced metalens demonstrates high transmittance and focusing ability as well as large depth of focus which makes it a promising solution for a new generation of silicon photomultiplier photodetectors with reduced fill factor impact on the performance and reduced electron-hole generation region, which altogether potentially leads to improved photodetection efficiency and other characteristics.

I. INTRODUCTION

Recent advances in nanofabrication technology resulted in the enhanced interest to light manipulation with flat nanostructured components - metasurfaces[1]. Due to high technological potential, the field of metasurfaces was booming during the last decade resulting in a variety of design ideas and description methods. Besides, metasurfaces keep finding more and more promising applications including miniature integrated devices such as on-chip spectrometers[2], camera objectives[3], compact integrated microscopes[4,5], etc. For many of them, it is of special interest to study wavefront shaping metasurfaces, in particular, metalenses.

Currently, the main metalens designs are based on arrays of nanoparticles and can be roughly classified depending on their size with respect to the wavelength. The first class of metalens use nanoparticles in a resonant regime which allows controlling scattering phase varying resonators shape, size, placement, and composition[6,7]. The second class of metalens employs nanoparticles in an off-resonant sub-wavelength regime. In this case, the metasurface can be described with a locally varying effective refractive index, and focusing is achieved by introducing the geometric phase difference into the beam[8–10]. We further concentrate only on all-dielectric structures as they are known to demonstrate better efficiency[11]. One of the most efficient types of metasurfaces is Huygens metasurface based on the modes interference within Mie-resonant high refractive index particles[12]. Although metasurfaces of this type were also designed for visible domain[13], the operation wavelength choice is significantly limited by the lack of lossless high-index materials in this range. In addition, due to their resonant nature, these metasurfaces are narrow-band.

On the other hand, devices based on a geometric phase manipulation are advantageous for the broadband operation. The way to design them works with sub-wavelength resonators arranged in a particular way. In case of devices based on a Berry phase,[14–17] resonators are anisotropic and the phase gradient is introduced by rotating them at a different angle. These metalenses operate only with circularly polarized light which, however, was shown to be beneficial for broadband imaging applications. For the design of polarization-independent components, resonators are chosen to be symmetric and vary only in size. Although such metasurfaces are described using different formalisms: light propagation in fundamental-mode waveguides[18,19], scattering on sub-wavelength diffraction grating[20–22], or gradient index (GRIN) surfaces[23,24], they are all subject to the homogenization and can be described with effective parameters (in case of Berry phase - anisotropic effective refractive index, in other cases - gradient refractive index). Most of the suggested options of graded-index metasurfaces are designed with high aspect ratio dielectric posts which require a complex fabrication process[14,15,19]. In addition, most materials used before are not CMOS-compatible, such as titanium oxide or PMMA, which means the component can not be readily integrated into the more complex device.

Here we develop, fabricate, and characterize a flat metalens design featuring several key advantages. It is fully CMOS-compatible and requires only simple nanostructuring of the surface. The optical performance combines an excellent transmission with focusing on a submicron size spot. Moreover, our metalens is polarization-insensitive, operates over a large spectral bandwidth, and appears to be quite robust to nanofabrication deficiencies.While a similar design was recently introduced in the far infrared region of the spectrum where the fabrication is much easier,[25] here it is the first time that this approach is demonstrated in the visible spectral range. Our

[a)] Electronic mail: stefan.enoch@fresnel.fr

general design can be easily implemented on a large range of applications, notably to improve the photodetection efficiency of photodetector arrays, for example, of silicon photomultipliers which are increasingly used as photodetectors in many applications. Focusing the light onto the active region of a photodetector pixel is an efficient approach to reduce the negative impact of the limited fill factor and improve the photogenerated signal. We focus on a simple design based on the hyperbolic secant profile[23,25,26] which is one of the perfectly imaging index profiles derived from the Maxwell fish-eye distribution with transformation optics methods[27]. Our metalens design is suitable for many CMOS-compatible fabrication methods and accessible materials. In this work, it is produced with a fabrication process consisting of e-beam vapor deposition and Focused Ion Beam (FIB) milling using niobium pentoxide Nb_2O_5 material[28] which has a large transparency window in the optical domain and was earlier used for ultraviolet metasurfaces design[29].

II. RESULTS AND DISCUSSION

The metalens is designed as a 2D square grating of holes of different diameters milled into niobium pentoxide Nb_2O_5. Its refractive index and extinction coefficient measured by spectrophotometry combined with fitting using Tauc-Lorentz dispersion model are shown in Figure 1a. The design of the holes grating is schematically shown in Figure 1b, where the overall size is $4\mu m$, and the period is $250nm$. The focusing ability of the metalens is provided by a gradient of refractive index, which turns the planar incoming wavefront into a focusing spherical wavefront. The refractive index gradient is introduced following the hyperbolic secant distribution Eq. 1, where n_{eff} - effective refractive index of the metalens, n_0 - initial refractive index of the selected material, x - varying coordinate.

$$n_{eff}(x) = n_0 \cdot sech(\alpha x) \tag{1}$$

Parameter α is calculated with Eq. 2, where x_0 defines the lens size (it changes from $-x_0$ to x_0), and the n_{x0} is the value of the effective refractive index at the edge of the structure (at $x = x_0$). Although such structures are often designed in the cylindrical coordinates[23,25], we use the Cartesian system because we aim at applications integrating arrays of metalenses on arrays of pixelized photodetectors, which follow a square lattice.

$$\alpha = \frac{x}{x_0} \cdot \cosh^{-1} \frac{n_0}{n_{x0}} \tag{2}$$

To introduce the effective index profile, we perforate apertures of a varying diameter $d(x)$ calculated with Eq. 3, where p is the structure period and $F(x)$ is a filling fraction calculated using the Maxwell-Garnett mixing rule adjusted for the dielectric mixtures (Eq. 4)[30].

$$d(x) = \sqrt{(4/\pi)p^2\,(1 - F(x))} \tag{3}$$

$$F(x) = \frac{(n_{eff}(x)^2 - 1)}{(n_{eff}(x)^2 + 1)} \cdot \frac{(n_0^2 + 1)}{(n_0^2 - 1)} \tag{4}$$

It states that in a case of sub-wavelength inclusions it is possible to consider the material as a mixture of constituent parts, in our case - Nb_2O_5 and air. Many homogenization approaches were developed for this type of problem, but this simple technique already provides a sufficiently good description. Resulting effective refractive index profile is shown in Figure 1c, the profile calculated analytically with Eq.(1) is shown with a solid line and the actually simulated one - with points connected by a dashed line. Minimum aperture size was limited to $100nm$ in order to perform fabrication by FIB lithography without requiring to elaborate structures or fabrication. Therefore, in the central part of the lens, there is a mismatch between the ideal and the simulated profile. Once we have the refractive index variation, we select the metalens thickness $h = 510nm$ allowing to estimate the phase shift $\phi(r)$ introduced to the transmitted beam Eq. 5. For the chosen operation wavelength $\lambda = 590nm$ (which is a wavelength of operation of a typical silicon photomultiplier that we see as a potential application of this work) resulting ideal and actual phase profiles are shown together with the refractive index in Figure 1c.

$$\phi(r) = \frac{2\pi n(r) h}{\lambda_0} \tag{5}$$

First of all, the calculated meta-lens was simulated in CST Studio Suite (r) on an infinite borosilicate glass substrate ($n_{sub} = 1.52$) with a plane wave ($\lambda = 590nm$) coming at normal incidence. To demonstrate focusing, XZ- cross-section of the normalized intensity in the substrate below the metalens is plotted in Figure 1d. In addition, the XY- cross-section corresponding to the best focus position (white dashed line in Figure 1d) is shown in Figure 1e.

The designed metalens was fabricated using a Focused Ion Beam (FIB) milling technique. Scanning Electron Microscopy (SEM) image of the fabricated structure is shown in Figure 1f. Afterward, it was characterized by scanning optical microscopy with the metalens being illuminated from the air side ($\lambda = 570 - 610nm$), and focusing light in the substrate. For a full characterization, images were taken in several planes. First, in the XZ-plane (Figure 2a) showing the long focusing spot with the $5.8\mu m$ Full Width at Half Maximum (FWHM) along the propagation direction (which is a large depth of focus). Second, in the XY-plane (Figure 2b) at the best focus position shown with a white dashed line in Figure 2a. The difference between the best focal positions for simulated (Figure 1d) and measured (Figure 2a) lens can be explained by the overall bias in apertures sizes. Our simulations show, that increasing all the aperture sizes in 20% leads to the best focal position shift from $\approx 8.5\mu m$ to $\approx 5.7\mu m$ away from the lens.

The images in Figure 2a,b show that light transmitted through the metalens is focused within a $950nm$ by $770nm$ spot (4.5% of the total area) with maximum concentration factor $C \approx 5$ defined as the ratio of irradiance on the surface

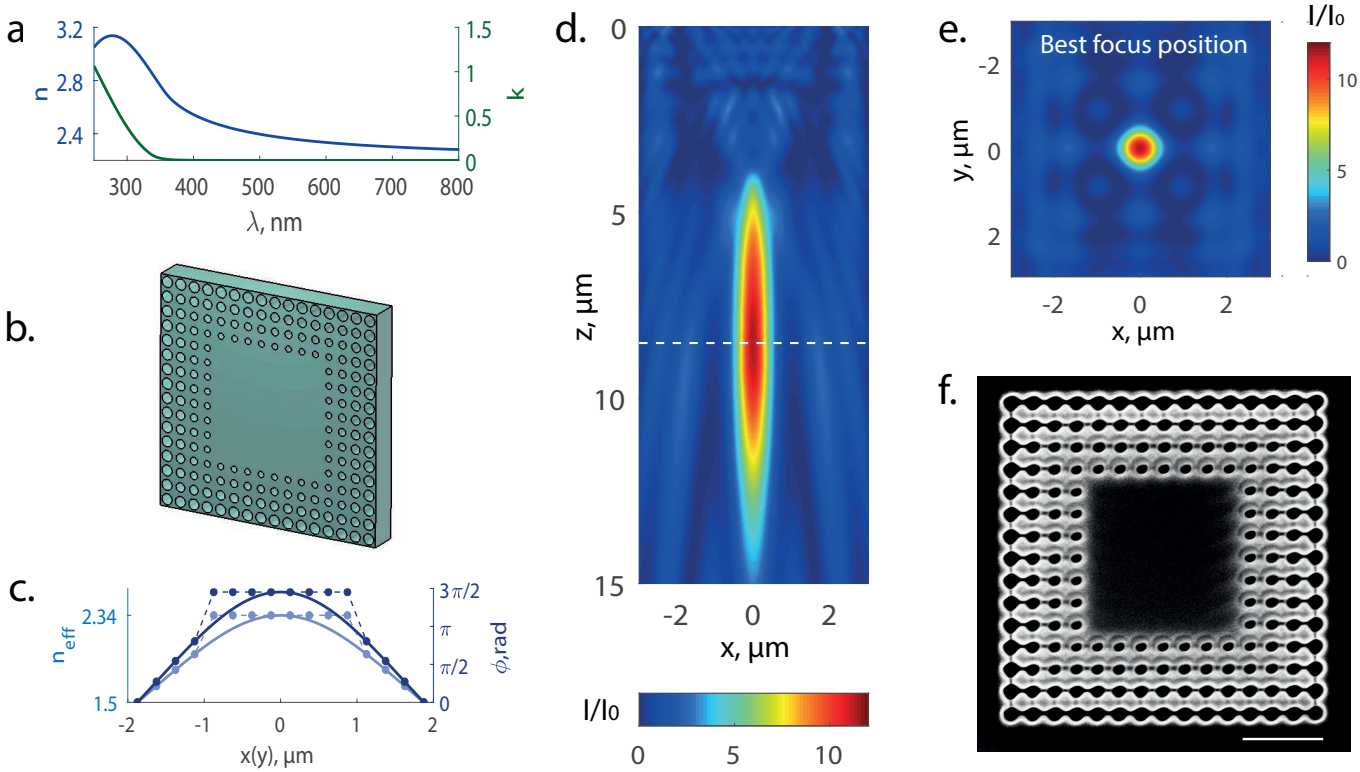

FIG. 1. (a) Niobium pentoxide Nb_2O_5 refractive index and extinction coefficient as a function of wavelength. (b) Schematic view of the designed meta-lens - square lattice with a refractive index gradient introduced by perforating apertures of varying diameters. Only apertures exceeding $100nm$ diameter were kept to simplify the fabrication: $d = 188nm$, $d = 161nm$, $d = 134nm$, and $d = 109nm$ considering the grating period $p = 250nm$. (c) In light blue - effective refractive index along the x- horizontal (or y- vertical) direction in (b), a solid line shows the profile calculated analytically using Eq. (1) and points joint by the dashed line - actually numerically simulated one. In dark blue – analytical and numerical phase profiles calculated for the metalens of the thickness $h = 510nm$ (d) Numerical modeling of the metalens performance. Normalized light intensity in the XZ-plane, the incident light intensity is used for normalization. The lens is simulated on a glass substrate $n_{sub} = 1.52$ with a plane wave of the wavelength $\lambda = 590nm$ sent from the vacuum on the top of the image along the z-direction. (e) Normalized light intensity in the XY-plane at the best focus position $x = 8.52\mu m$ (dashed white line in (d)). (f)SEM image of the metalens fabricated by FIB-lithography, the scale bar is 1 μm

of the concentrator to the irradiance in the detection region[31] which is equivalent to the ratio of intensities in this case[32]. Slight astigmatism between X- and Y-axis indicated by the 20% difference in their respective FWHM values is not an effect due to polarization (we use a non-polarized halogen lamp) but is rather connected to the slightly asymmetric shape of the holes milled in the metalens (SEM image Fig. 1f). Nevertheless, without any post-processing of the image (deconvolution from the microscope point spread function) and despite some nanofabrication imperfections, the focus spot remains below 1 μm^2. Finally, several XY-crosscut images were recorded at several z positions: best focal position $f - 4\mu m$, $f + 4\mu m$, $f + 6\mu m$ to fully characterize the propagation Figure 2c). Altogether, the data in Fig. 2 demonstrate the excellent optical performance of our simple and scalable metalens design. The system is also robust to the minor nanofabrication defects. Contrarily to resonant metasurfaces, our refractive index gradient approach does not require perfect control on each hole size or position. Metalens performance is also illustrated with a video (supporting information) demonstrating white light (halogen lamp, λ from 500 to $650nm$) focusing: the XY-crosscut of the image was taken at different Z-coordinates varying from 0 to $15\mu m$ and back. In the video, there are 6 samples with different milling depths ranging from $\approx 400nm$ deep (on the left) to $\approx 500nm$ (on the right), the second sample from the right is the metalens shown in Figure 2. This video confirms metalens excellent performance in the bright field with spectral range from 500 to $650nm$.

To assess the restrictions induced by the limited minimum size of the holes milled into niobium pentoxide, we model the metalens considering apertures of diameters $d > 20nm$ (Figure 3a for XZ-crosscut, and Figure 3f for XY-crosscut). In this case, the observed focal spot is smaller in comparison to the design with $d > 100nm$ (Figure 3b and Figure 3g respectively.) However, due to the choice of the square lattice, a small part of the light is directed away from the focus which results in the decrease of the intensity enhancement. Therefore, for a given geometry, limitation to sizes bigger than $100nm$ does not hamper the optical performance, and can even improve slightly the peak intensity at the focus. Then, to study broadband behavior of the metalens

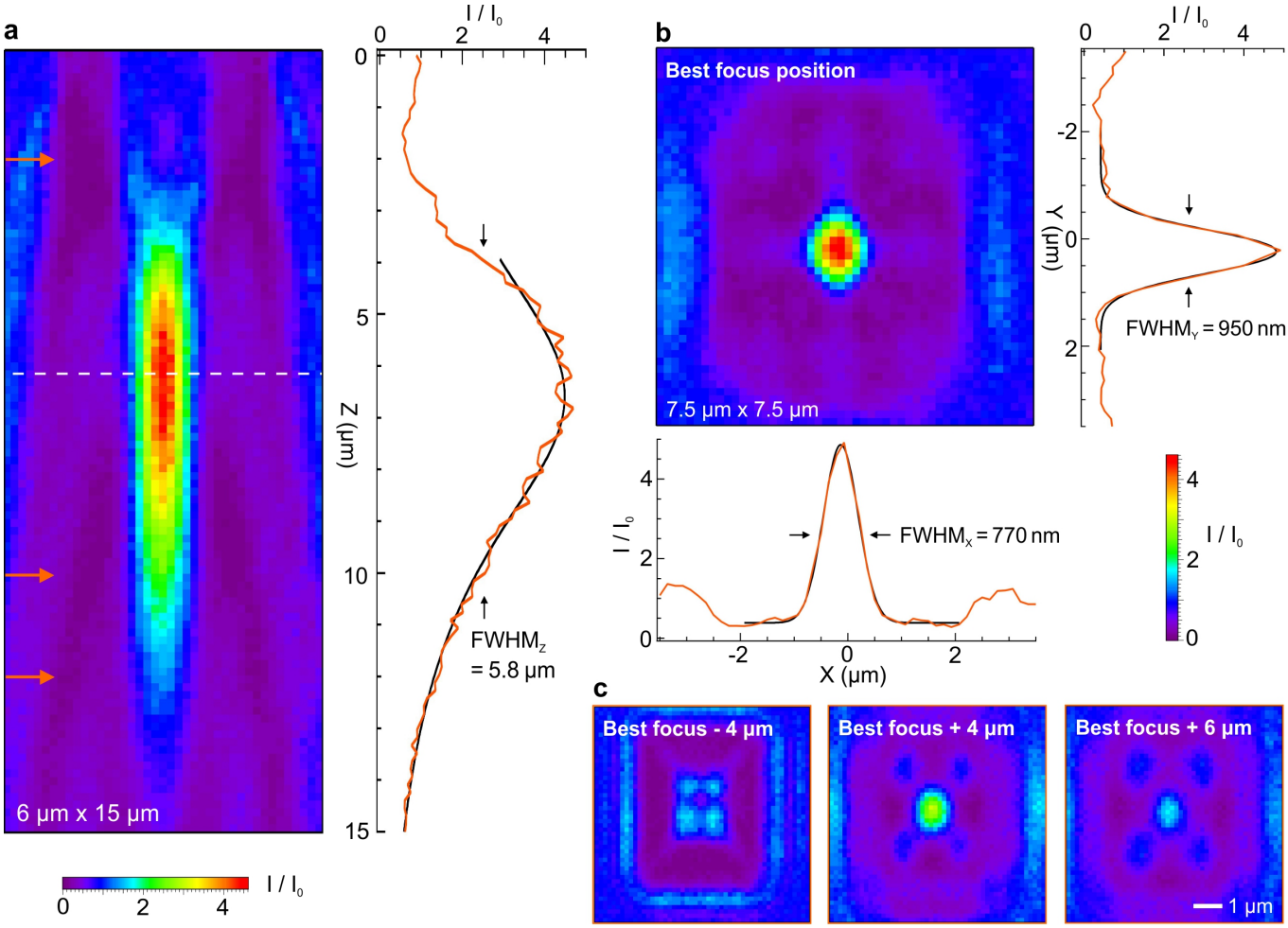

FIG. 2. Experimental characterization of the metalens. (a) Scanning optical microscope image along the XZ-plane parallel to the light propagation. The illumination is provided by a collimated beam from a white lamp spectrally filtered at $590 \pm 20nm$ incoming from the top of the image. The intensity is normalized by the incoming light intensity in the absence of the structure. The graph on the right shows a crosscut along the vertical direction at the center of the focus. The orange line is experimental data and the black line is a fit using a Lorentzian function. (b) Microscope image recorded at the best focus position (dashed white line in (a)) along the XY-plane perpendicular to the beam propagation. The graphs show crosscuts of the focus spot along the two main directions. Orange lines are experimental data while black lines are Gaussian fits used to determine the spot full width at half maximum (FWHM). (c) Images recorded in the transverse plane at different distances from the best focus position (defined in (b)), corresponding to the positions indicated by the orange arrows in (a). All the images in (a-c) share the same color scale.

with $d > 100nm$ it was simulated at several wavelengths $\lambda = 490nm, 540nm, 590nm, 640nm, 690nm$. Results (Figure 3c) show that, although the maximum focal spot shifts along the z-direction, the intensity enhancement stays high in the broad wavelength range, and, in case of a photodetection application, the detection region could be placed in such a way that electron-hole generation probability would be optimal in a large wavelength region.

To estimate the sensitivity to the fabrication error, we simulate the metalens with $d > 100nm$ (Figure 1b) with the aperture diameter taken randomly from the normal distribution with a standard deviation $\sigma = 10nm$, where the mean value is a calculated diameter for a given spatial point ($188nm$, $161nm$, $134nm$, or $109nm$). Results (Figure 3d) show no major decrease in the intensity enhancement which further demonstrates the design robustness. Then, to analyze the effect of non-verticality of the fabricated apertures, we simulate metalens using truncated cones instead of the cylinders with perfectly vertical walls - the top base diameter equal to d, and the bottom one - to $0.6d$. Figure 3e shows that this leads to a non-negligible intensity enhancement decrease which, however, matches better with the measurement results Figure 2a. Finally, we simulate the unit cells with the different aperture diameters using periodic boundaries to compute transmittance amplitude and phase. These two quantities calculated in the case of cylindrical and conical apertures are shown in Figure 3h as a function of the aperture diameter d. The difference in the phase profiles explains the focusing efficiency drop in the case of the conical apertures, which is straightforwardly explained with the homogenization model as well,

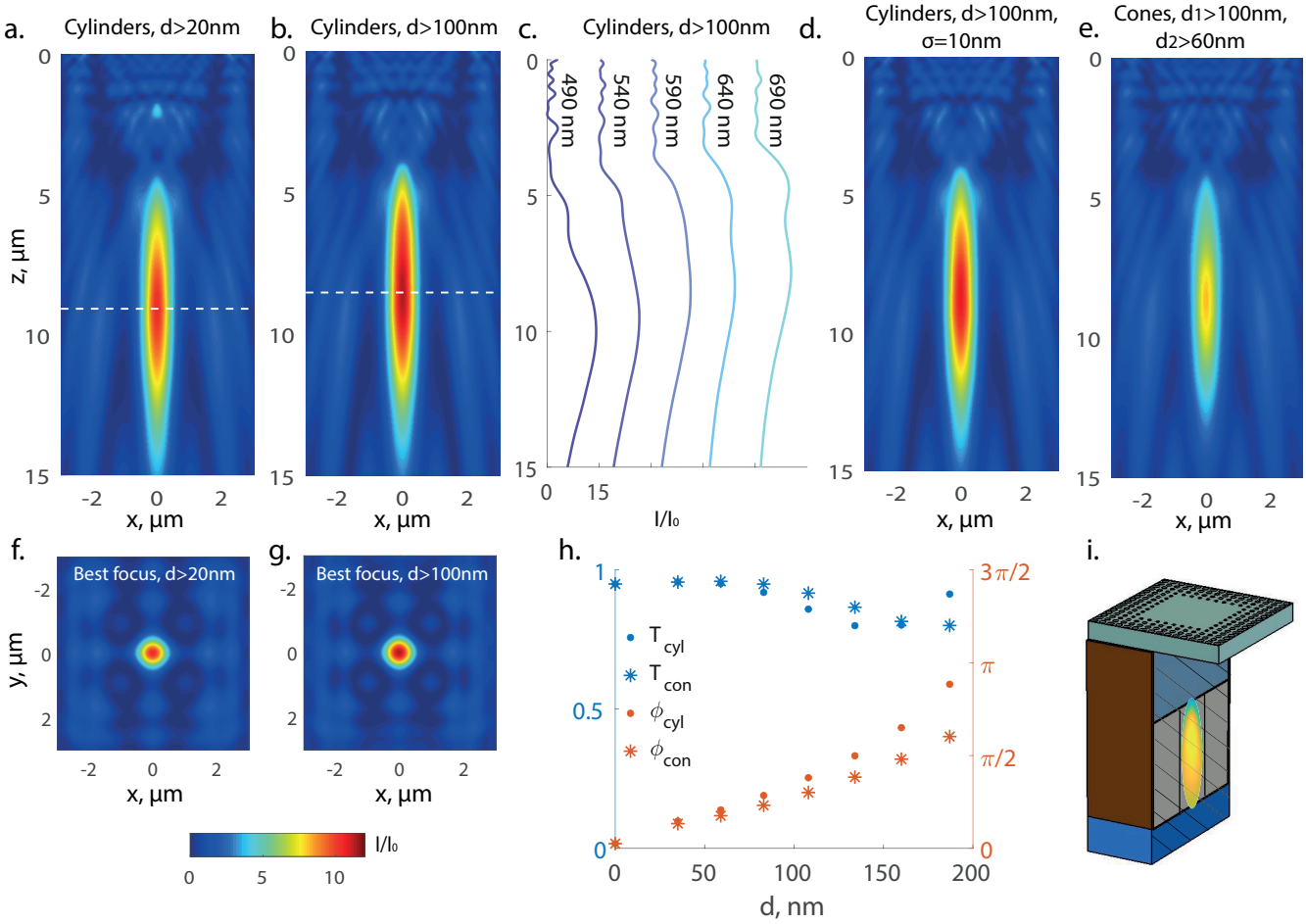

FIG. 3. Metalens numerical modeling (In all cases, $n_{sub} = 1.52$, a plane wave sent from the vacuum on the top of the image along the z-direction. For all the figure parts except (c) $\lambda = 590nm$. (a) Normalized light intensity in the XZ-plane for the metalens with aperture diameters $d > 20nm$ (b) Normalized light intensity in the XZ-plane for the metalens with aperture diameters $d > 100nm$ (c) A crosscut along the vertical direction at the center of the focus corresponding to the simulation made for different wavelengths. Result for $\lambda = 590nm$ correspond to the normalized intensity from (b) along the line $x = 0$. (d) Normalized light intensity in the XZ-plane for the metalens with $d > 100nm$ where the diameter is taken randomly from the normal distribution with a mean value d and a standard deviation $\sigma = 10nm$.(e) Normalized light intensity in the XZ-plane for the metalens with truncated cones as apertures - the top base diameter equal to d, and the bottom one - to 60% of d.(f) Normalized light intensity in the XY-plane at the best focus position $x = 8.52\mu m$ in case of design with aperture diameters limited to values $d > 20nm$ (dashed while line in (a)) (g) Normalized light intensity in the XY-plane at the best focus position $x = 8.52\mu m$ in case $d > 100nm$ (dashed white line in (b)). (h) Numerical simulation of the amplitude and phase of the light transmitted through a periodic metasurface with the apertures of the identical diameter to determine the local response from the different metalens areas. Simulation was done for different diameters d in case of cylindrical and conical apertures. (i) Illustration of metalens application: reducing the amount of light that would hit the dead boarder of the single photon avalanche photodiode by focusing it in the center of the detection region

as it changes mixture proportions and results in a smaller effective refractive index contrast. Moreover, results shown in Figure 3h allow calculating average transmittance amplitude which is $T \approx 0.93$ in case of cylindrical apertures for both profiles with $d > 20nm$ and $d > 100nm$, and in case of conical once with $d > 100nm$.

To demonstrate the scalability of our design, we investigated the potential of a Fresnel metalens composed of 8 different concentric sections (Figure 4). The purpose of these sections is, as in a regular Fresnel lens, to enable a short focal length together with a large lens diameter without requiring too thick materials. The fabricated Fresnel metalens of dimensions $17 \times 17\mu m^2$ has been characterized with the same method as the metalens in Figure 2. The optical microscope images taken at the metalens surface and at its best focus plane are shown in Figure 4b,c. From the axial shift between these two planes, we deduce that this Fresnel metalens has a focal length of $7\mu m$. Considering the $17\mu m$ dimension of the lens and the 1.5 refractive index of the medium where the light is focused, this Fresnel metalens features an impressive numerical aperture of 1.15. While the concentric sections intrinsic to the Fresnel design introduce interference ripples around the focal spot (as we work under spatial coherent condition with plane wave illumination), the focal spot still bears transverse

dimensions well below $1\mu m$ demonstrating efficient focusing. Crosscuts through the focal spot along the horizontal (Figure 4d) and the vertical (Figure 4e) directions indicate better the intensity distribution. A local intensity enhancement about 8 together with FWHM of $800nm$ show the ability of the lens to concentrate light in a tiny spot. Comparing our results with other approaches, high-index microspheres were demonstrated to focus visible and infrared light into spots of approximately one wavelength[33,34] or even half a wavelength[35–37] in FWHM. Besides, silicon cones were used for mid-infrared and long-infrared photodetectors.[38] Solid immersion metalens achieved a FWHM of about $2\ \lambda$[39], while monolithically integrated metalenses also focus infrared light into spots of one wavelength in FWHM[40]. Here our results achieved in the visible spectral range are at the same level than the state-of-the-art for flat components.

III. CONCLUSIONS

We have developed a polarization-independent broadband efficient metalens and fabricated it with CMOS - compatible technology. Our results show that metasurface transmits light with high transmission efficiency (estimated as $T \approx 0.93$) which is then focused on a $950nm$ by $770nm$ spot occupying $\approx 4.5\%$ of the total area in the center below it with 5 folds maximum concentration factor reached. The focusing spot is spanning for $5.8\mu m$ in the z-direction which leaves flexibility for the detection region choice.

The produced metalens can be used for improving the photodetection efficiency (PDE) of silicon photomultipliers by reducing the amount of light that would hit the non-active area at the edge of the single-photon avalanche photodiode (SPAD) which is equivalent to reducing the influence of the fill factor (FF) on the PDE[41]. The situation is illustrated in Figure 3i where the light that was supposed to enter the non-efficient zone close to the border is concentrated in a center of the detection region. Apart from reducing the influence of the FF, focusing light in a small area should allow creating a smaller electron-hole generation region which is beneficial for the avalanche generation and signal formation homogeneity. Our metalens design is a step towards $\approx 100\%$ FF light detection, it also gives the opportunity to increase the width of the dead border even in very small cells ($\leq 5\mu m$). This approach is fully scalable and can be easily integrated with any pixelized photodetector array.

IV. METHODS

A. Numerical modeling

All simulations are performed using the commercially available software CST Studio Suite (r). The entire metalens was simulated with the Transient solver based on the Finite Integration Technique (FIT). These simulations were done using "open" boundary conditions in x- and y- directions which correspond to a single lens perforated in the film infinite in x- and y- directions. To reduce the computation time, we set the background media to be glass $n = 1.52$ and artificially fill apertures and the space above the metalens with the vacuum. The excitation source is a plane wave (linearly polarized light with the electric field along x-direction) coming from the vacuum side and a field monitor "Power" is set allowing extracting the maximum value of the Poynting vector (P) within one period of time as a function of the coordinate. Finally, we compute spatial distribution of the transmission coefficient as a ratio between the Poynting vector calculated in presence and in absence of the metalens. This method is equivalent to calculating the transmission coefficient as a ratio of field intensities[32]. The unit cell performance as a function of the aperture diameter was simulated using a Frequency-domain solver combining finite elements method with special broadband frequency sweep techniques. We used a Unit cell boundary condition that considers a periodic structure and provides a complex transmission coefficient as a result.

B. Nanofabrication

A $510nm$ thick layer of Nb_2O_5 was deposited on glass substrates using plasma-assisted electron beam deposition (Bühler SYRUSpro 710). High density, high uniformity layer was achieved using this technique. The precise thickness was monitored using in-situ direct optical monitoring (Bühler OMS 5000) at $550nm$. A thin $10nm$ additional aluminum layer was deposited on top of the Nb_2O_5 layer using the same technology but unassisted to make the structure conductive and remove electrical charges during etching. The metalens concentrator design used for the numerical simulations was converted using a MATLAB code to generate the pattern compatible with the focused ion beam system (FEI dual-beam DB235 Strata). The pattern was milled using a focused ion beam with a gallium-based source using 30 keV energy and a $10pA$ beam current. Scanning electron microscopy images were performed at $5keV$ energy with SFEG source of the electron column.

C. Optical characterization

Optical microscopy experiments are based on a home-made microscope system derived from a confocal setup reproducing the conditions used in[35]. The illumination uses the in-built halogen lamp from the Nikon Eclipse inverted microscope. The field and aperture diaphragms are closed to the maximum so that the light beam emerging from the condenser lens illuminating the sample is nearly collimated. The sample containing the metalens is illuminated from the air side, and the apertures milled in the niobium pentoxide are filled with air. The characterization of the light focused by the metalens is performed from the borosilicate glass substrate (refractive index of substrate 1.52). We use a Zeiss C-Apochromat $63 \times 1.2NA$ infinity-corrected water-immersion objective to image the metasurface lens focus. A $30\mu m$ pinhole conju-

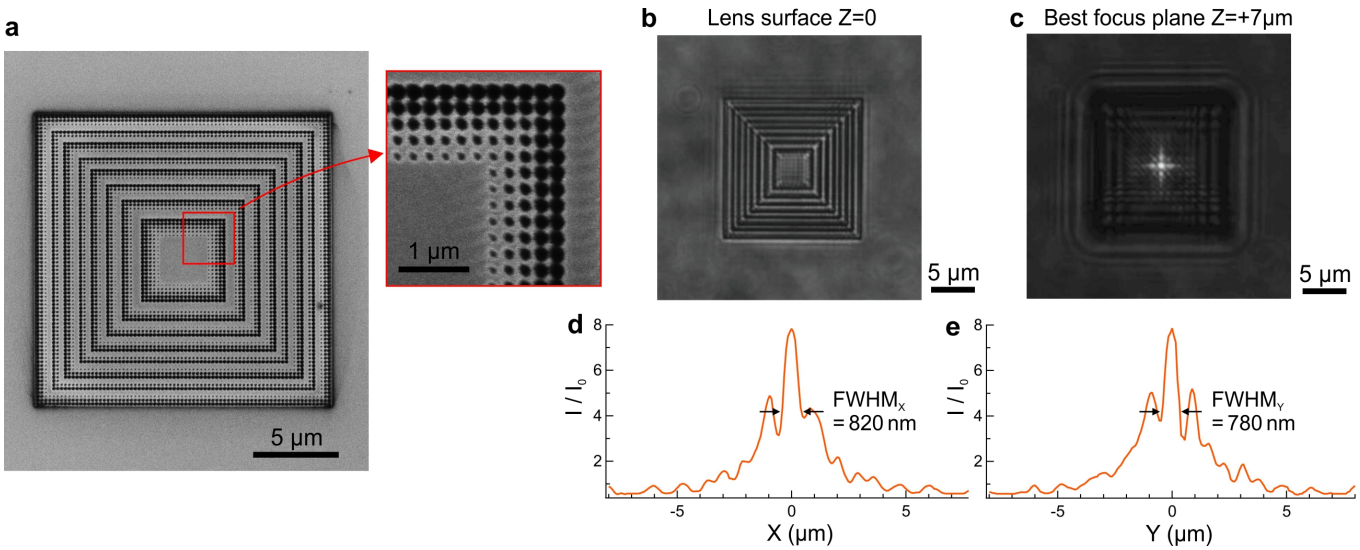

FIG. 4. Fresnel metalens with nanoholes milled in niobium pentoxide layer. (a) SEM image of the fabricated sample. 8 different concentric section are present. The insert shows a high magnification view of one quarter of the central section. (b) Optical microscope image of the Fresnel metalens taken when the microscope focus is set on the Nb_2O_5 layer corresponding to the metalens surface. (c) Optical microscope image taken at the best focus of the metalens, $7\mu m$ below the metalens surface. (d,e) Crosscuts of the intensity of the image (c) along the x- and y- directions. The intensity is normalized by the light intensity outside the lens (edge of image (b)).

gated with the microscope objective focus plane using a 164 mm Zeiss tube lens defines the confocal detection volume and provides the lateral and axial sectioning. A 3-axis piezo stage (Polytec PI P-517.3CD) scans the sample respective to the fixed detection and illumination. The intensity measurement is performed with an avalanche photodiode (MPD-5CTC, Picoquant) positioned after the pinhole connected to a photon counting module (Hydraharp 400, Picoquant). A bandpass filter (ZET405 /488 /565 /640mv2, Chroma) selects only the light in the 570-610 nm spectral window.

STATEMENT OF AUTHOR CONTRIBUTION

E.M. and S.E. conceived the design, E.M performed theoretical and numerical calculations, J.L. provided technical support on the materials and coordinated the deposition of the Nb_2O_5 thin film, .J.B.C. fabricated the sample, J.W. characterized the sample, M.S. conceived and planned the Photoquant project, M.S., M.P., P.L., E.A., S.E. and A.G. supervised and coordinated the project, A.F., A.G. and G.P. provided technical support on the photodetector structure and requirements, E.M. wrote the manuscript with support from J.W., S.E., R.A. , J.L., and M.S. All authors provided critical feedback and revised the manuscript.

SUPPLEMENTARY MATERIAL

Please see *Zscan_whitelamp_subtitles.mp*4: a video demonstrating the white light propagation $15\mu m$ below 6 metalens samples with varying milling depth.

DATA AVAILABILITY

The data that support the findings of this study are available from the corresponding author upon reasonable request.

ACKNOWLEDGMENTS

This work was done in the frame of the project Photoquant, which has received funding from the ATTRACT project funded by the EC under Grant Agreement 777222. This project was initiated by the ERC Advanced Grant TICAL (grant agreement No 338953). This project has received funding from the European Research Council (ERC) under the European Union's Horizon 2020 research and innovation program (grant agreement No 723241)

[1] S. B. Glybovski, S. A. Tretyakov, P. A. Belov, Y. S. Kivshar, and C. R. Simovski, "Metasurfaces: From microwaves to visible," Physics Reports **634**, 1–72 (2016).
[2] A. Leitis, A. Tittl, M. Liu, B. H. Lee, M. B. Gu, Y. S. Kivshar, and H. Altug, "Angle-multiplexed all-dielectric metasurfaces for broadband molecular fingerprint retrieval," Science Advances **5**, eaaw2871 (2019).
[3] A. Arbabi, E. Arbabi, S. M. Kamali, Y. Horie, S. Han, and A. Faraon, "Miniature optical planar camera based on a wide-angle metasurface doublet corrected for monochromatic aberrations," Nature Communications **7**, 13682 (2016).
[4] H. Kwon, E. Arbabi, S. M. Kamali, M. Faraji-Dana, and A. Faraon, "Single-shot quantitative phase gradient microscopy using a system of multifunctional metasurfaces," Nature Photonics **14**, 109–114 (2020).
[5] E. T. F. Rogers, J. Lindberg, T. Roy, S. Savo, J. E. Chad, M. R. Dennis, and N. I. Zheludev, "A super-oscillatory lens optical microscope for subwavelength imaging," Nature Materials **11**, 432–435 (2012).
[6] N. Yu and F. Capasso, "Flat optics with designer metasurfaces," Nature materials **13**, 139–150 (2014).
[7] M. Khorasaninejad and F. Capasso, "Metalenses: Versatile multifunctional photonic components," Science **358** (2017).

[8] P. Lalanne and P. Chavel, "Metalenses at visible wavelengths: Past, present, perspectives: Metalenses at visible wavelengths: Past, present, perspectives," Laser & Photonics Reviews **11**, 1600295 (2017).

[9] P. Genevet, F. Capasso, F. Aieta, M. Khorasaninejad, and R. Devlin, "Recent advances in planar optics: From plasmonic to dielectric metasurfaces," Optica **4**, 139 (2017).

[10] S. M. Kamali, E. Arbabi, A. Arbabi, and A. Faraon, "A review of dielectric optical metasurfaces for wavefront control," Nanophotonics **7**, 1041–1068 (2018).

[11] A. I. Kuznetsov, A. E. Miroshnichenko, M. L. Brongersma, Y. S. Kivshar, and B. Luk'yanchuk, "Optically resonant dielectric nanostructures," Science **354**, aag2472 (2016).

[12] M. Decker, I. Staude, M. Falkner, J. Dominguez, D. N. Neshev, I. Brener, T. Pertsch, and Y. S. Kivshar, "High-Efficiency Dielectric Huygens' Surfaces," Advanced Optical Materials **3**, 813–820 (2015).

[13] Y. F. Yu, A. Y. Zhu, R. Paniagua-Domínguez, Y. H. Fu, B. Luk'yanchuk, and A. I. Kuznetsov, "High-transmission dielectric metasurface with 2π phase control at visible wavelengths: High-transmission dielectric metasurface with 2π phase control at visible wavelengths," Laser & Photonics Reviews **9**, 412–418 (2015).

[14] R. C. Devlin, M. Khorasaninejad, W. T. Chen, J. Oh, and F. Capasso, "Broadband high-efficiency dielectric metasurfaces for the visible spectrum," Proceedings of the National Academy of Sciences **113**, 10473–10478 (2016).

[15] M. Khorasaninejad, W. T. Chen, R. C. Devlin, J. Oh, A. Y. Zhu, and F. Capasso, "Metalenses at visible wavelengths: Diffraction-limited focusing and subwavelength resolution imaging," Science **352**, 1190–1194 (2016).

[16] S. Wang, P. C. Wu, V.-C. Su, Y.-C. Lai, M.-K. Chen, H. Y. Kuo, B. H. Chen, Y. H. Chen, T.-T. Huang, J.-H. Wang, R.-M. Lin, C.-H. Kuan, T. Li, Z. Wang, S. Zhu, and D. P. Tsai, "A broadband achromatic metalens in the visible," Nature Nanotechnology **13**, 227–232 (2018).

[17] B. Groever, W. T. Chen, and F. Capasso, "Meta-Lens Doublet in the Visible Region," Nano Letters **17**, 4902–4907 (2017).

[18] S. Vo, D. Fattal, W. V. Sorin, Z. Peng, T. Tran, M. Fiorentino, and R. G. Beausoleil, "Sub-Wavelength Grating Lenses With a Twist," IEEE Photonics Technology Letters **26**, 1375–1378 (2014).

[19] M. Khorasaninejad, A. Y. Zhu, C. Roques-Carmes, W. T. Chen, J. Oh, I. Mishra, R. C. Devlin, and F. Capasso, "Polarization-Insensitive Metalenses at Visible Wavelengths," Nano Letters **16**, 7229–7234 (2016).

[20] P. Lalanne, S. Astilean, P. Chavel, E. Cambril, and H. Launois, "Design and fabrication of blazed binary diffractive elements with sampling periods smaller than the structural cutoff," Journal of the Optical Society of America A **16**, 1143 (1999).

[21] A. Zhan, S. Colburn, R. Trivedi, T. K. Fryett, C. M. Dodson, and A. Majumdar, "Low-Contrast Dielectric Metasurface Optics," ACS Photonics **3**, 209–214 (2016).

[22] M. Ye, Y. Peng, and Y. S. Yi, "Silicon-rich silicon nitride thin films for subwavelength grating metalens," Optical Materials Express **9**, 1200 (2019).

[23] T.-M. Chang, S. Guenneau, J. Hazart, and S. Enoch, "Focussing light through a stack of toroidal channels in PMMA," Optics Express **19**, 16154 (2011).

[24] P. R. West, J. L. Stewart, A. V. Kildishev, V. M. Shalaev, V. V. Shkunov, F. Strohkendl, Y. A. Zakharenkov, R. K. Dodds, and R. Byren, "All-dielectric subwavelength metasurface focusing lens," Optics Express **22**, 26212 (2014).

[25] J. Moughames, S. Jradi, T. M. Chan, S. Akil, Y. Battie, A. E. Naciri, Z. Herro, S. Guenneau, S. Enoch, L. Joly, J. Cousin, and A. Bruyant, "Wavelength-scale light concentrator made by direct 3D laser writing of polymer metamaterials," Scientific Reports **6**, 33627 (2016).

[26] N. Kundtz and D. R. Smith, "Extreme-angle broadband metamaterial lens," Nature Materials **9**, 129–132 (2010).

[27] K. Mantel, D. Bachstein, and U. Peschel, "Perfect imaging of hypersurfaces via transformation optics," Optics Letters **36**, 199 (2011).

[28] W. Cote, M. Slocum, S. Chandra, M. Fredell, and T. Rahmlow, "Optical properties, morphology and temperature influence of SiO_2, Nb_2O_5 and HfO_2 films as a function of ion energy and process," in *Optical Interference Coatings* (Optical Society of America, 2016) pp. ThC–7.

[29] K. Huang, J. Deng, H. S. Leong, S. L. K. Yap, R. B. Yang, J. Teng, and H. Liu, "Ultraviolet Metasurfaces of ≈80% Efficiency with Antiferromagnetic Resonances for Optical Vectorial Anti-Counterfeiting," Laser & Photonics Reviews **13**, 1800289 (2019).

[30] A. Sihvola, "Mixing Rules with Complex Dielectric Coefficients," Subsurface Sensing Technologies and Applications **1**, 393–415 (2000).

[31] S. Donati, G. Martini, and M. Norgia, "Microconcentrators to recover fill-factor in image photodetectors with pixel on-board processing circuits," Optics Express **15**, 18066 (2007).

[32] H. A. Macleod, *Thin-Film Optical Filters*, 4th ed., Series in Optics and Optoelectronics (CRC Press/Taylor & Francis, Boca Raton, FL, 2010) pp. 18–20, 26, oCLC: ocn176924832.

[33] K. W. Allen, F. Abolmaali, J. M. Duran, G. Ariyawansa, N. I. Limberopoulos, A. M. Urbas, and V. N. Astratov, "Increasing sensitivity and angle-of-view of mid-wave infrared detectors by integration with dielectric microspheres," Applied Physics Letters **108**, 241108 (2016).

[34] F. Abolmaali, A. Brettin, A. Green, N. I. Limberopoulos, A. M. Urbas, and V. N. Astratov, "Photonic jets for highly efficient mid-ir focal plane arrays with large angle-of-view," Optics express **25**, 31174–31185 (2017).

[35] P. Ferrand, J. Wenger, A. Devilez, M. Pianta, B. Stout, N. Bonod, E. Popov, and H. Rigneault, "Direct imaging of photonic nanojets," Optics Express **16**, 6930 (2008).

[36] B. S. Luk'yanchuk, R. Paniagua-Domínguez, I. Minin, O. Minin, and Z. Wang, "Refractive index less than two: photonic nanojets yesterday, today and tomorrow," Opt. Mater. Express **7**, 1820–1847 (2017).

[37] A. Maslov and V. Astratov, "Resolution and reciprocity in microspherical nanoscopy: Point-spread function versus photonic nanojets," Phys. Rev. Applied **11**, 064004 (2019).

[38] B. Jin, G. W. Bidney, A. Brettin, N. I. Limberopoulos, J. M. Duran, G. Ariyawansa, I. Anisimov, A. M. Urbas, S. D. Gunapala, H. Li, and V. N. Astratov, "Microconical silicon mid-ir concentrators: spectral, angular and polarization response," Opt. Express **28**, 27615–27627 (2020).

[39] S. Zhang, A. Soibel, S. A. Keo, D. Wilson, S. B. Rafol, D. Z. Ting, A. She, S. D. Gunapala, and F. Capasso, "Solid-immersion metalenses for infrared focal plane arrays," Applied Physics Letters **113**, 111104 (2018).

[40] F. Li, J. Deng, J. Zhou, Z. Chu, Y. Yu, X. Dai, H. Guo, L. Chen, S. Guo, M. Lan, *et al.*, "Hgcdte mid-infrared photo response enhanced by monolithically integrated meta-lenses," Scientific reports **10**, 1–10 (2020).

[41] G. Zappalà, F. Acerbi, A. Ferri, A. Gola, G. Paternoster, V. Regazzoni, N. Zorzi, and C. Piemonte, "Study of the photo-detection efficiency of FBK High-Density silicon photomultipliers," Journal of Instrumentation **11**, P11010–P11010 (2016).

[42] F. Acerbi, A. Gola, V. Regazzoni, G. Paternoster, G. Borghi, N. Zorzi, and C. Piemonte, "High Efficiency, Ultra-High-Density Silicon Photomultipliers," IEEE Journal of Selected Topics in Quantum Electronics **24**, 1–8 (2018).

[43] G. Zappalà, F. Acerbi, A. Ferri, A. Gola, G. Paternoster, V. Regazzoni, N. Zorzi, and C. Piemonte, "Study of the photo-detection efficiency of FBK High-Density silicon photomultipliers," Journal of Instrumentation **11**, P11010–P11010 (2016).

[44] X. Ni, A. V. Kildishev, and V. M. Shalaev, "Metasurface holograms for visible light," Nature Communications **4**, 2807 (2013).

[45] W. Stork, N. Streibl, H. Haidner, and P. Kipfer, "Artificial distributed-index media fabricated by zero-order gratings," Optics Letters **16**, 1921 (1991).

[46] G. H. Yuan, E. T. Rogers, and N. I. Zheludev, "Achromatic super-oscillatory lenses with sub-wavelength focusing," Light: Science & Applications **6**, e17036–e17036 (2017).

[47] Z. Zhou, J. Li, R. Su, B. Yao, H. Fang, K. Li, L. Zhou, J. Liu, D. Stellinga, C. P. Reardon, T. F. Krauss, and X. Wang, "Efficient Silicon Metasurfaces for Visible Light," ACS Photonics **4**, 544–551 (2017).